Microstructural evolution of cobalt-doped barium cerate–zirconate at elevated temperatures under moist reducing conditions

Joysurya Basu [*], Aravind Suresh [1], Benjamin A. Wilhite [1], C. Barry Carter

Department of Chemical, Materials & Biomolecular Engineering, 191 Auditorium Road, University of Connecticut, Storrs 06269, CT, USA

Abstract

Barium cerates doped with rare earth and transition metal ions are attractive candidate materials for clean-energy applications owing to their catalytic activity combined with mixed ionic–electronic conductivity for electrochemical hydrogen separation. However, the stability of these materials at elevated temperatures in the presence of moisture and CO_2 is not completely understood. In the present work, Co-doped barium cerate–zirconate pellets ($BaCe_{0.25}Zr_{0.47}Co_{0.13}O_{3-\delta}$) were exposed to a moist reducing environment at 600 °C and 927 °C for 24 h. The as-sintered and reduced pellets were sectioned using FIB and characterized using conventional TEM, STEM and XEDS. The evolution of the microstructure of the material at each step has been reported. The as-sintered material showed a tendency toward Co ex-solution resulting in the formation of a BaO–CoO phase at the grain boundaries. At elevated temperatures, reduction appeared to play a role in the transformation of the material chemistry and microstructure. © 2011 Elsevier Ltd. All rights reserved.

Keywords: Fuel cells; Membranes; Perovskites; Electron microscopy; Microstructure-final

1. Introduction

Diminishing fossil-fuel resources, increasing energy demands and environmental concerns have accelerated the search for alternative energy technologies capable of integration with both existing and emerging infrastructures. Polymer electrolyte membrane fuel cells (PEMFCs) operating using high-purity hydrogen are considered one of the most viable of such technologies, as hydrogen fuel may be produced from solar, wind and nuclear power via water electrolysis with a net-zero carbon footprint, or from existing fossil and emerging biomass-derived fuels. High-purity hydrogen is harvested from hydrocarbon fuels (e.g., coal, ethanol) via a combination of catalytic reforming (e.g., endothermic steam reforming and exothermic partial oxidation) and subsequent purification.[1,2]

Product purification is critical, as CO and other reforming by-products (e.g., H_2S, CO_2) have deleterious effects on fuel cell performance and lifetime.[3,4]

Dense Pd films are currently the leading technology for achieving high (>1000:1) perm-selectivity toward hydrogen purification; however high material cost combined with the inability to drive hydrogen permeation rates via external electric fields (i.e., galvanic mode) limit their economic viability.[5] Electro-ceramics may provide a promising alternative to Pd for hydrogen purification, if the materials are suitably stable at elevated temperatures (400–800 °C) in reducing environments.

Solid-oxide fuel cells (SOFCs) operating at temperatures in excess of 600 °C allow for the internal reforming of hydrocarbon fuels while avoiding the deleterious effects of CO and CO_2 experienced by PEMFCs, thus removing the need for hydrogen purification. Current SOFC materials are based upon yttria-stabilized zirconia (YSZ) which requires operating temperatures of 1000 °C or more, owing to limited ionic conductivity. The development of new electro-ceramics for SOFCs has been driven by the need to reduce operating temperatures by 100 °C or more in order to mitigate material degradation and sealing challenges.[6,7] Emerging materials must be suit-

* Corresponding author. Present address: Physical Metallurgy Division, Indira Gandhi Center for Atomic Research, Kalpakkam 603102, TN, India. Tel.: +91 0979 167 3025; fax: +91 0442 748 0202.

E-mail address: jbasu@igcar.gov.in (J. Basu).

[1] Present address: Artie McFerrin Department of Chemical Engineering, Texas A&M University, College Station, TX 77843, USA.
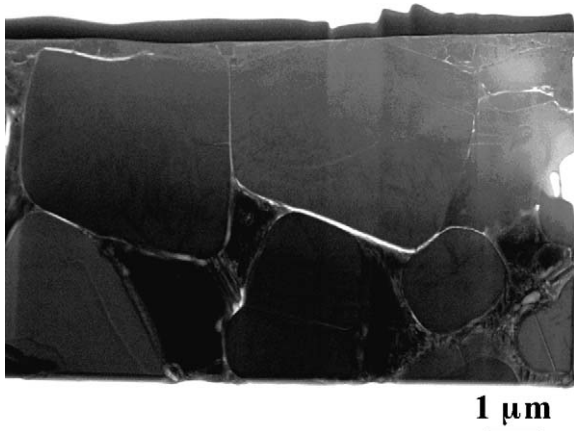
Fig. 1. FIB section of the Co-doped barium cerate–zirconate pellet after sintering at 1550 °C for 12 h.

ably stable under reducing conditions at elevated temperatures (600–900 °C).

The ABO_3 family of perovskites ($SrCeO_3$, $BaCeO_3$, $CaZrO_3$, $SrZrO_3$) has emerged as a promising alternative for addressing both hydrogen purification and SOFC challenges, with potential applications as electrolytes and in hydrogen sensors, steam concentrators, steam electrolysis, hydrogenation and dehydrogenation of organic compounds.[8–11] Doped barium cerates display combinations of protonic and oxygen-ion conductivities between 400 and 800 °C, with certain dopants introducing additional electronic conductivity.[12] Recently, our research team demonstrated that promising catalytic activity may be imparted through catalytically active transition metal dopants.[13] This combination of electrochemical and catalytic properties at intermediate temperatures makes barium cerates applicable in both SOFCs and hydrogen purification systems.

Different synthesis methods for pure and doped barium cerates and ceria have been reported in the literature as have their electrical properties.[14–18] It has been reported that barium cerates exhibit limited chemical stability under CO_2 and H_2O environments, decomposing into $BaCO_3/CeO_2$ and

$Ba(OH)_2/CeO_2$ respectively.[19,20] Other studies have reported adequate practical stability of Gd-doped barium cerates under SOFC operating environments.[21–23] This indicates that the temperature, CO_2/H_2O partial pressures in the environment and the type of dopant all play a role in determining the stability of barium cerate. Doping with Zr, for example, has been reported to be a viable solution to provide a compromise between chemical stability and electrical conductivity of the cerate.[18]

In order to reduce the maintenance cost of SOFCs and in turn reduce the cost of energy, it is important to understand the stability and the course of degradation of the applied materials. A mechanistic understanding of the microstructural changes that occur during the process of degradation may generate useful insight for better design of the materials. The present work aims at understanding the microstructural and the chemical changes of Co doped barium cerate–zirconate under moist reducing conditions at 600 °C and 927 °C.

2. Experimental procedure

Cobalt-doped barium cerate–zirconate powder with a target composition of $BaCe_{0.25}Zr_{0.60}Co_{0.15}O_{3-\delta}$ was synthesized by oxalate co-precipitation. The precipitate, initially amorphous, was heat-treated at 1550 °C for 4 h. Based on XRD (X-ray diffraction) and STEM–XEDS studies, the heat-treated powder was observed to be chemically homogeneous with a single-phase cubic structure. The details of the synthesis and the structural and functional characterization have been reported elsewhere.[13] Subsequent to the initial study,[13] elemental analysis was performed on the dried precipitate obtained after the oxalate co-precipitation synthesis. The technique of inductively coupled plasma-optical emission spectrometry (ICP-OES) was used to determine the Ba/Ce, Ba/Zr and Ba/Co mole ratios in the material.

The heat-treated powder was compacted at room temperature at ∼100 MPa and the green compact was sintered at 1550 °C for 12 h with heating and cooling rates of 5 °C/min. The sintered pellets were reduced in a 10% wet hydrogen environment
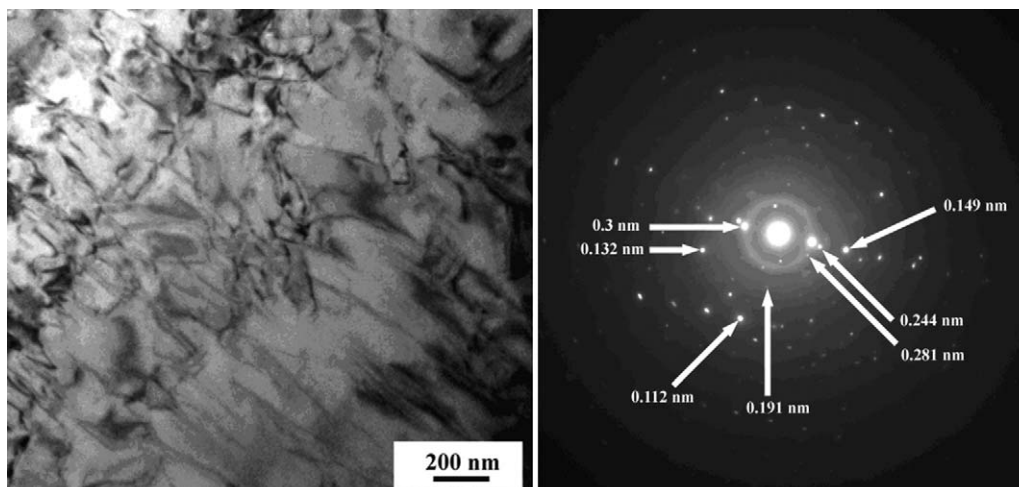

Fig. 2. TEM image of the Co-doped barium cerate–zirconate sintered sample and the diffraction pattern. Array of dislocation and defects proves the crystalline nature of the Co doped barium cerate–zirconate phase.
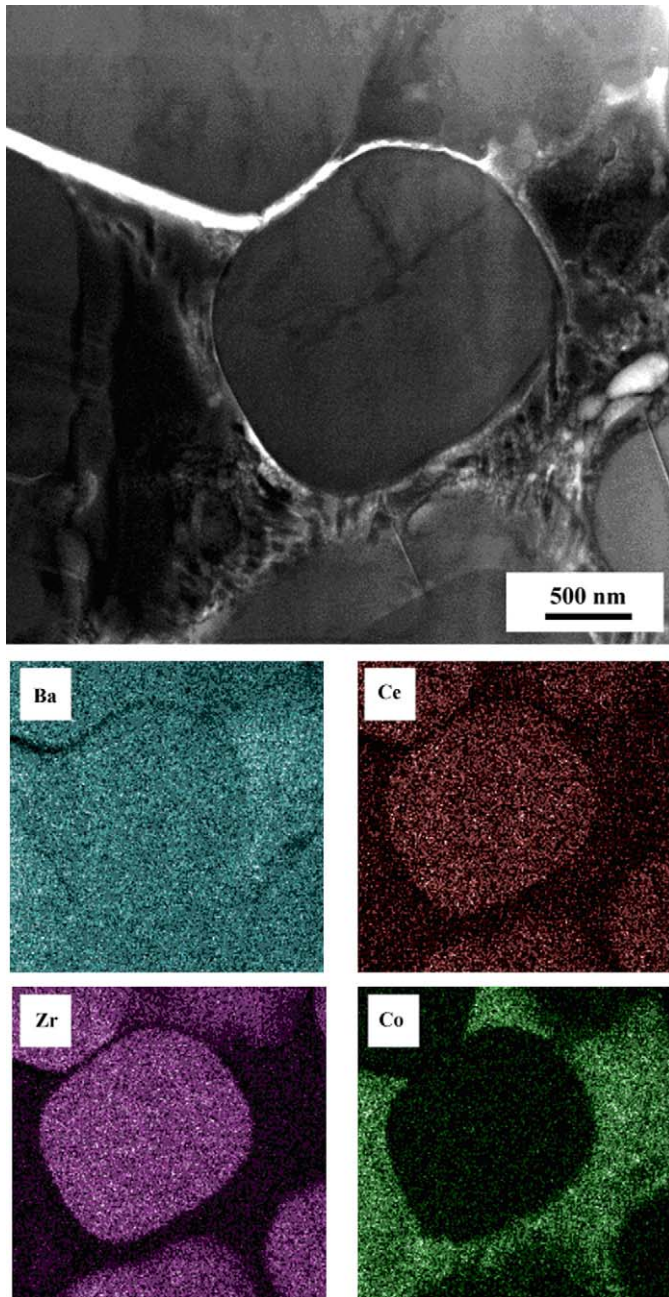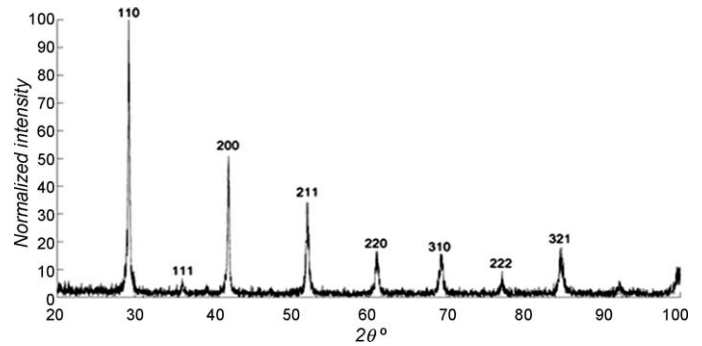
Fig. 4. X-ray diffraction pattern of the Co-doped barium cerate–zirconate pellet after sintering at 1550 °C for 12 h. In the diffraction pattern, presence of any other phase except the cubic barium cerate–zirconate phase could not be found.

3. Results

Crystalline, homogeneous barium cerate–zirconate was obtained by heat treatment of the precipitate synthesized by oxalate co-precipitation. Elemental analysis of the precipitate was performed using ICP-OES. Assuming that the Ba/Ce, Ba/Zr and Ba/Co mole ratios remained constant after the heat treatment, the actual composition of the heat-treated powder was determined to be closer to $BaCe_{0.25}Zr_{0.47}Co_{0.13}O_{3-\delta}$, with an A:B ratio > 1 as compared to the targeted composition of $BaCe_{0.25}Zr_{0.60}Co_{0.15}O_{3-\delta}$, with an A:B ratio ~1.

The TEM image of the FIB section of the as-sintered sample is given in Fig. 1. The Pt layer, visible at the top surface of the pellet, had reduced in thickness during the course of the ion-beam thinning. The interface between the Pt layer and the pellet was straight and well defined indicating a smooth surface morphology of the pellet. The sintered pellet was polycrystalline with widely varying grain sizes in the range of 1–5 μm. The grains were faceted with well defined grain boundaries. Minor cracks in the intergranular boundary regions were observed. A different contrast was observed in some of the intergranular regions indicating the presence of a second phase. A high-magnification image of one of the grains and the diffraction pattern from the sample are given in Fig. 2. In the high-magnification image of the grain, a high density of defects typical of brittle ceramics was observed. This observation, in conjunction with the presence of spots in the diffraction pattern, indicated the presence of crystalline phases in the sintered pellet. The d-spacings, as measured from the diffraction pattern and marked in Fig. 2, match with those corresponding to the cubic barium cerate–zirconate phase as reported in an earlier paper.[13] The lattice parameter of this phase is very close to pure cubic $BaCeO_3$ and cubic $BaZrO_3$ phases. Several diffraction spots indicative of the presence of CoO were observed. Some of the spots indicated the presence of CeO_2 and BaO in minor quantities. A detailed analysis of the d-spacings is given in Table 1. As some of the d-spacings of these phases are quite similar to those of the barium cerate–zirconate phase, additional chemical mapping would be required to confirm their presence.

The STEM image and the chemical maps for a representative cross-section of the as-sintered sample are given in Fig. 3. A cross-section displaying multiple grains and the intergranular

Fig. 3. STEM–EDS map of the sintered Co-doped barium cerate–zirconate FIB section. Localized Co ex-solution takes place at the grain boundaries.

(P_{H2O} ~4.18 kPa (31 Torr)) for 24 h at 600 °C and 927 °C respectively. In order to study the reactive nature of the pellet in this environment, the exposed surface of the reduced pellets was coated with a ~5 μm thick platinum layer and a vertical section was lifted out in the form of a membrane with an FEI Strata 400S FIB. A section from an as-sintered sample was also lifted out in order to provide a reference. The vertical sections were thinned to electron-transparency by a Ga ion beam. The electron-transparent samples were characterized using a Tecnai T12 TEM operated at 120 kV. The chemical nature of the samples was characterized using a STEM–XEDS attachment on the same microscope.
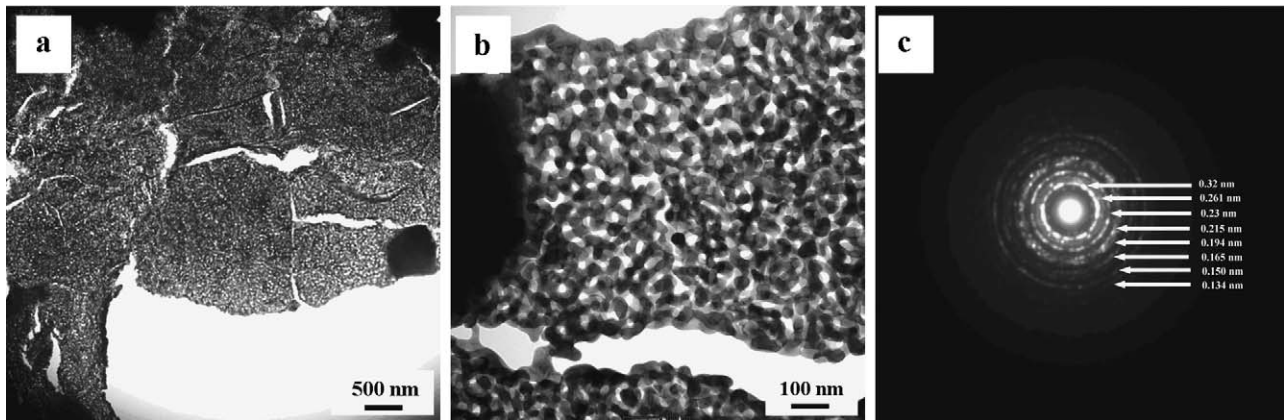
Fig. 5. TEM image and electron diffraction pattern of the sintered Co-doped barium cerate–zirconate sample reduced in 10% wet H_2 environment for 24 h at 600 °C. Cracks form at the grain boundaries and the mottled contrast starts appearing at the grain bodies.

Table 1
Analysis of the observed d-spacings from the FIB section of the pellet sintered at 1550 °C for 12 h.

Observed d-spacings (nm)	Reported d-spacings (nm) cF8 BaO	Reported d-spacings (nm) cF8 CoO	Reported d-spacings (nm) cF12 CeO$_2$	Reported d-spacings (nm) cP5 BaCeO$_3$	Reported d-spacings (nm) cP5 BaZrO$_3$
0.3	0.319 (111)		0.312 (111)	0.314 (110)	0.296 (110)
0.281	0.276 (200)		0.270 (200)		
0.244		0.246 (111)		0.222 (200)	0.242 (111)
0.191	0.195 (220)		0.191 (220)	0.181 (332)	0.187 (210)
0.149		0.150 (220)		0.157 (220)	0.148 (220)
0.132	0.127 (331)	0.128 (311)	0.135 (400)	0.128 (222)	0.132 (310)
0.112	0.113 (422)	0.106 (400)	0.113 (422)	0.118 (321)	0.112 (321)

regions was selected in order to observe any inhomogeneity in the material. It is observed from Fig. 3 that Ba was uniformly present across the sample without any particular tendency of segregation. Ce and Zr tended to be located primarily with the grains, while Co showed a predominant tendency of segregating at the grain boundaries. Thus, it appears that heat treatment of the pressed powder led to Co segregation in the form of CoO at the grain boundaries. Barium is also present at the grain boundaries in the form of BaO. Conversely, faint signals from Ce and Zr observed at the grain boundaries indicate only very small quantities of CeO$_2$–ZrO$_2$. Thus, STEM–XEDS analysis of the as-sintered material indicates a BaO–CoO intergranular region. However, XRD patterns of the polished surfaces of an as-sintered pellet, given in Fig. 4, did not indicate the presence of a second phase, suggesting that any intergranular phase is below the detection limit of X-ray diffraction technique. These observations of localized mal-distribution of Ce, Zr and Co in the sintered material contrast to previous STEM–XEDS analysis of heat-treated powders[13] which displayed a uniform distribution of all three B-site cations.

The TEM image and the diffraction pattern of the FIB section of the pellet reduced at 600 °C for 24 h are given in Fig. 5a–c. After reduction at 600 °C the grain structure was still visible though with a considerable change in the grain contrast. The intergranular cracks had grown considerably and a mottled contrast was observed in TEM images of grains. In the high mag-

nification image of a grain (Fig. 5b) a typical river-like pattern could be observed suggesting the occurrence of a hydrolysis process. The analysis of the diffraction pattern (Fig. 5c) indicated the presence of the original phase along with crystalline cubic
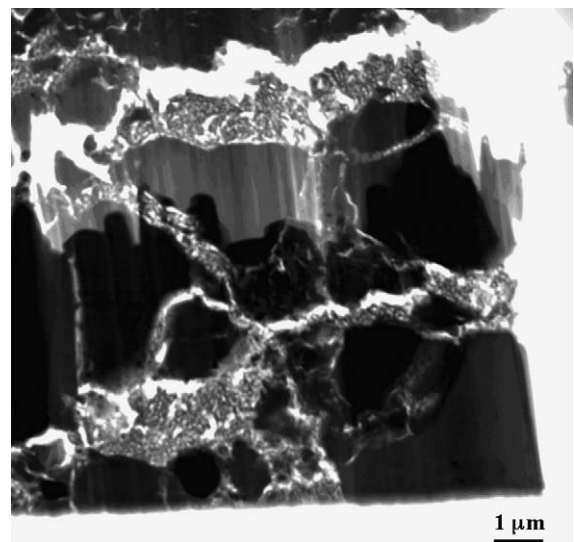

Fig. 6. STEM image of the sintered Co-doped barium cerate–zirconate sample reduced in 10%wet H_2 environment for 24 h at 927 °C. Along with cracks at the grain boundaries localized mesh like structure forms indicating a reactive nature of the sample.
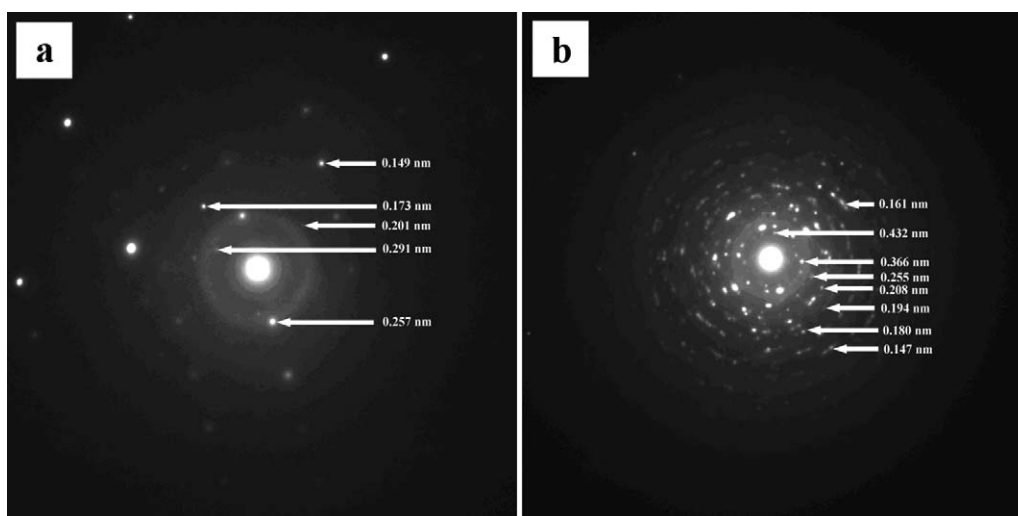
Fig. 7. Electron diffraction pattern from the (a) grain and (b) the mesh-like region in the sample reduced at 900 °C. Both of the morphologically different phases are crystalline. The grains are still barium cerate–zirconate phase whereas the mesh like structure is a combination of BaO and CeO$_2$ phases.

Table 2
Analysis of the observed d-spacings from the FIB section of the pellet reduced at 600 °C for 24 h.

Observed d-spacings (nm)	Reported d-spacings (nm) cP5 BaCeO$_3$	Reported d-spacings (nm) cP5 BaZrO$_3$	Reported d-spacings (nm) cF8 BaO	Reported d-spacings (nm) cF12 CeO$_2$	Reported d-spacings (nm) cF8 CoO
0.32	0.314 (110)	0.296 (110)	0.319 (111)	0.312 (111)	
0.261	0.256 (111)		0.276 (200)	0.270 (200)	
0.23	0.222 (200)				0.246 (111)
0.215		0.209 (200)			0.213 (200)
0.194	0.181 (211)	0.187 (210)	0.195 (220)	0.191 (220)	
0.165	0.157 (220)	0.171 (211)	0.167 (311)	0.163 (311)	
0.150	0.140 (310)	0.148 (220)	0.159 (222)	0.156 (222)	0.150 (220)
0.134	0.128 (222)	0.132 (310)	0.138 (400)	0.135 (400)	0.128 (311)

CoO, BaO and CeO$_2$. The detailed analysis of the diffraction pattern is given in Table 2. However, STEM–XEDS mapping could not detect any locally segregated regions of BaO, CoO or CeO$_2$ with certainty. Extensive formation of intergranular cracks after reduction at 600 °C resulted in a loss of the Co-rich boundary region observed in the as-sintered sample. The interface between the Pt layer and the surface of the pellet was still visible (Fig. 5a) but the top surface was no longer smooth and well defined, indicating a considerable amount of surface reaction.

The TEM image of the FIB section of the pellet reduced at 927 °C for 24 h is given in Fig. 6. A considerable structural change from the as-sintered pellet was observed. Two morphologically distinguishable regions, consisting of grains and an intergranular mesh-like structure were observed. Diffraction patterns corresponding to the grains (Fig. 7a) and the intergranular mesh-like structure (Fig. 7b) are presented separately. Detailed analysis of the diffraction patterns in Fig. 7a and b is given in Table 3 and Table 4, respectively. It is apparent from the diffrac-

tion patterns that both regions were crystalline. The diffraction pattern from the grains indicated the presence of cubic barium cerate–zirconate with the d-spacings very close to the values reported for BaCeO$_3$ and BaZrO$_3$, while that from the mesh-like region indicated the presence of BaO, CeO$_2$ and CoO along with the barium cerate–zirconate phase. It has been mentioned

Table 3
Analysis of the diffraction pattern from a grain in the FIB section of the pellet reduced at 927 °C for 24 h.

Observed d-spacings (nm)	Reported d-spacings (nm) cP5 BaCeO$_3$	Reported d-spacings (nm) cP5 BaZrO$_3$
0.291		0.296 (110)
0.257	0.256 (111)	0.242 (111)
0.201	0.198 (210)	0.209 (200)
0.173	0.181 (211)	0.171 (211)
0.149	0.148 (300)	0.148 (220)

Table 4
Analysis of the diffraction pattern from the intergranular region from the FIB section of the pellet reduced at 927 °C for 24 h.

Observed d-spacings (nm)	Reported d-spacings (nm) cF8 BaO	Reported d-spacings (nm) cF8 CoO	Reported d-spacings (nm) cF12 CeO$_2$	Reported d-spacings (nm) cP5 BaCeO$_3$	Reported d-spacings (nm) cP5 BaZrO$_3$
0.432				0.444 (100)	0.419 (100)
0.366			0.312 (111)	0.314 (110)	
0.255	0.276 (200)	0.246 (111)	0.270 (200)	0.256 (111)	0.242 (111)
0.208		0.213 (200)		0.222 (200)	0.209 (200)
0.194	0.195 (220)		0.191 (220)	0.198 (210)	0.187 (210)
0.180				0.181 (211)	0.171 (211)
0.161	0.167 (311)		0.163 (311)	0.157 (220)	
0.147	0.159 (222)	0.150 (220)	0.156 (222)	0.148 (300)	0.148 (220)

earlier that some of the d-spacings of BaO, CoO and CeO$_2$ are very close to that of barium cerate–zirconate phase. It requires STEM–XEDS chemical mapping to confirm their presence with certainty.

The FIB-sectioned sample was chemically mapped by STEM–XEDS (Fig. 8). The region for chemical mapping was chosen such that the grain body, intergranular cracks and the mesh-like structures were all mapped simultaneously. Ba was uniformly distributed throughout the sample without any indication of segregation. Ce and Zr were located primarily with the grains, whereas Co had almost completely segregated into localized regions along the grain boundaries. This observation confirms that the grains are barium cerate–zirconate. In the mesh-like grain boundary region CoO is present alongside a combination of barium cerate–zirconate, BaO and CeO$_2$. These phases appear to be homogeneously mixed.

4. Discussion

Pure and doped barium cerate is an attractive material for clean-energy applications. Several methods have been reported in the literature for synthesizing barium cerate[13,15] and barium zirconate[24,25] for energy applications. For the oxalate co-precipitation technique employed in the present study, the precipitate phase was initially amorphous, becoming crystalline upon high-temperature heat treatment. This is in contrast to the amine precipitation routes which produce crystalline precipitates. Crystalline powders were found to be comprised of a homogeneous cubic phase via XRD analysis with uniform distribution of Ba, Ce, Zr and Co. Elemental analysis of precipitates indicated a composition of $BaCe_{0.25}Zr_{0.47}Co_{0.13}O_{3-\delta}$, corresponding to a high (13 mol%) doping of Co and a 1.18:1 excess of A-site to B-site cations. Details regarding the analysis of the as-synthesized powders have been previously reported.[13] The present analysis of the sintered pellets of this material provides further understanding of the stability and microstructure upon sintering and after exposure to moist reducing environments.

In spite of being a very attractive candidate material, Co-doped barium cerate–zirconate with this particular chemistry is not completely stable under the reaction environment. It has been observed that the surface is flat initially and the surface starts
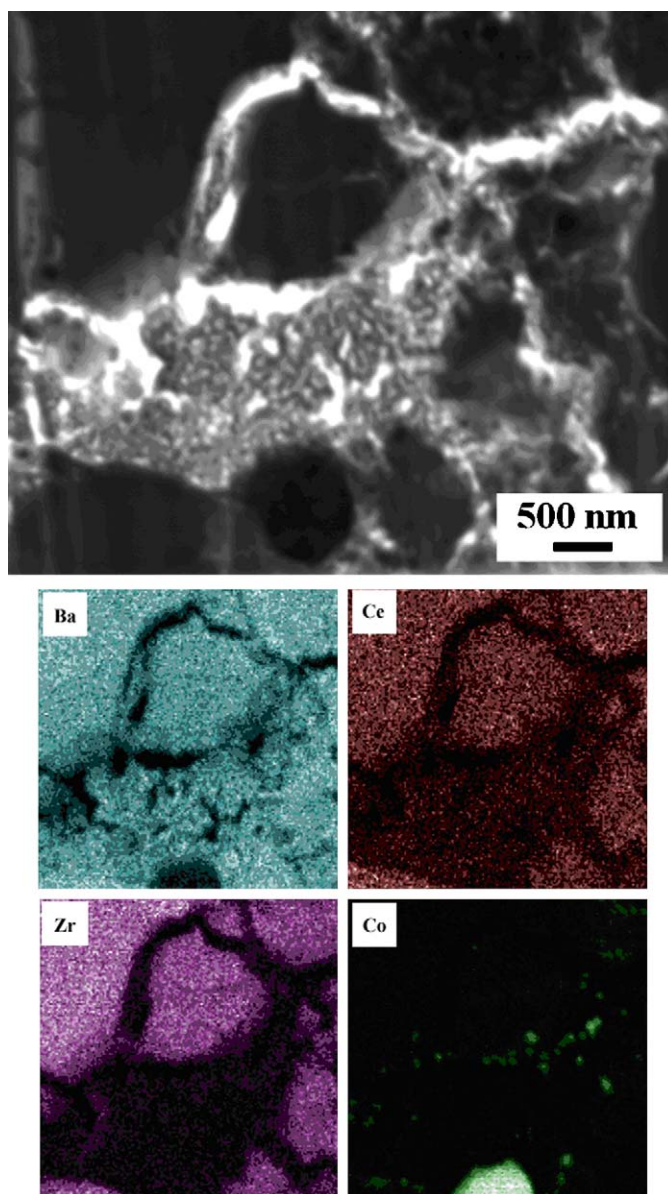

Fig. 8. STEM–EDS map of the sample reduced at 927 °C for 24 h. Hydrolysis and separation of chemical species can be observed.

to react with the reaction mixture leading to an undulated surface morphology. Formation of a reaction product on the surface has been reported elsewhere[21] but the prognosis of this reactive transformation process has not been studied in detail. Contrary to the reported literature, it has been observed that the degradation starts at the surface and it gradually propagates into the bulk material.[19] The surface becomes rough due to the degradation and then the grains inside the bulk material degrade leading to the grains with mottled contrast and intercrystalline mesh-like region.

It is proposed that there are several steps to the degradation process. In the as-sintered sample localized preferential segregation of Co and Ba can be observed at the grain boundaries. The degradation starts with the ex-solution of Co and Ba, which changes this single-phase homogeneous material into a segregated microstructure. It appears that solid-solubility limit of Co in Zr-doped BaCeO$_3$ is not very high which results in Co exsolution. It is not possible to determine the terminal solubility limit of Co due to the lack of phase-diagram data. Precipitation of BaO and CeO$_2$ has been reported earlier. It has also been reported that doping beyond a certain level results in precipitation of a second phase at the grain boundaries.[26]

In this work it has been observed that the precipitation takes place at the grain boundaries due to the hydrolysis process which results in the formation of an interconnected rod like region. There are pockets where Co segregates to the grain boundaries but Ce and Zr tend to stay within the grains. This transformation is not solely related to its reactive nature in the reducing environment. It is more thermodynamic in a sense that excess of Co beyond the solid solubility limit of barium cerate–zirconate tends to separate out and segregate at the grain boundary. The rest of the degradation process can be attributed to the reactive nature of the material under the reducing environment. In the diffraction patterns from the decomposed samples the signature of the BaO and CeO$_2$ phases can be obtained which can further be confirmed by the STEM–XEDS mapping. In the chemical maps Zr is invariably observed wherever Ce is present. This indicates that ZrO$_2$ is not an independent decomposition product. After decomposition of barium cerate–zirconate BaO and CeO$_2$ forms independently and Zr is present in CeO$_2$ in the form of solid solution. The mottled contrast that is observed with the grains, along with the 'flow lines', indicates an operative hydrolysis process in which barium cerate–zirconate is hydrolyzed to form ceria–zirconia solid solution and interconnected barium oxide nanorods. The nanorods are ∼100–500 nm long and 10–50 nm in width.

Hydrothermal synthesis of BaO nanostructures has not been reported in the literature. It has, however, been reported that pure BaCeO$_3$ decomposes in the presence of H$_2$O vapor by the following reaction[19]:

$$BaCeO_3 \quad (s) + H_2O \quad (g) \rightarrow CeO_2 \quad (s) + Ba(OH)_2 \quad (s/l) \tag{1}$$
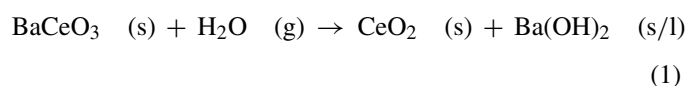
The change in free energy associated with this reaction has been determined.[19] As the present material has been addition-

ally doped with Zr, those free energy equations will not hold exactly. Moreover, the physical state of Ba(OH)$_2$ is ambiguous. It is presumed that Ba(OH)$_2$, not being a very stable hydroxide, will further decompose into BaO and H$_2$O. In the present study, the presence of CeO$_2$ and BaO have both been observed; these are presumably the dehydrated products. The water of dehydration further decomposes the unaltered barium cerate–zirconate grains, advancing the decomposition process from the grain boundary into the grain body. Wu and Liu[21] have also investigated surface reactivity of Gd-doped barium cerate in a moist environment. However, their observation on Ba(OH)$_2$ was quite different from the present study as they studied powder samples; the original morphology was therefore not retained under the microscope. Their conventional imaging technique was unable to detect any kind of interface between reacted and unreacted material, and they concluded that no decomposition occurred under moisture.

The tendency of this material to react with moisture and hydrogen may be explained using defect reactions and the Kroger–Vink notation, with the underlying assumptions of Ba (+2) being the A-site cation and Zr (+4), Co (+2) and Ce (+4) being situated at the B-sites. In a Ba-excess composition, Ce or Zr vacancies may form and subsequently react with Ba to form barium oxide by the following mechanism:

$$Ba_{Ba} + V_{Ce/Zr}'''' + 2\,V_O^{\bullet\bullet} + O_O^X \rightarrow BaO \tag{2}$$

$$BaO + H_2O \rightarrow Ba(OH)_2 \tag{3}$$
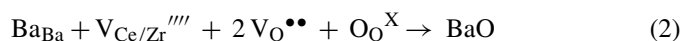
The hydrolysis of barium may occur due to moisture in the vapor phase or due to moisture dissolved in the material:

$$H_2O + V_O^{\bullet\bullet} + O_O^X \rightarrow 2OH^\bullet \tag{4}$$

The latter mechanism of hydrolysis would explain the difference in degradation between 600 and 927 °C, specifically that the grain structure remains visible after exposure to H$_2$/H$_2$O at 927 °C while significant decomposition of individual grains is observed at 600 °C, as moisture solubility is expected to decrease with increasing temperature.

In the case of a cobalt-doped composition, cobalt ex-solution to form cobalt oxide may occur via interactions of cobalt (substituted at the zirconium and cerium B-cation sites) with oxygen vacancies and lattice oxygen as follows:

$$Co_{Zr/Ce}'' + V_O^{\bullet\bullet} + O_O^X \rightarrow CoO + V_{Co}'' \tag{5}$$
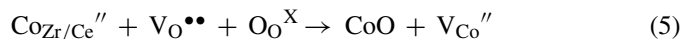
CoO may undergo reduction in the presence of hydrogen to form metallic Co:

$$CoO + H_2 \rightarrow H_2O + Co \tag{6}$$
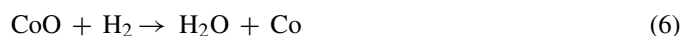
The remaining cobalt vacancy may react with A-site barium to form barium oxide:

$$Ba_{Ba} + V_{Co}'' + V_O^{\bullet\bullet} + O_O^X \rightarrow BaO \tag{7}$$
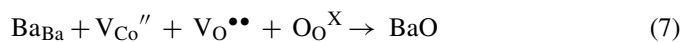
Which may then react with moisture to form barium hydroxide following Eq. (3). The mechanism detailed in Eqs. (2)–(4) would be expected to occur in any doped barium cerate–zirconate with A:B > 1 but in this specific material it would be expected to occur

additionally owing to the presence of cobalt as the dopant, via the reduction mechanism presented in Eqs. (5)–(7).

The stability of this class of ceramics would be expected to depend strongly upon both the extent of cobalt doping and the initial A:B ratio in the material. The present experimental results and hypothesized mechanisms for decomposition provide a framework for more detailed decomposition studies aimed at validating Eqs. (2)–(7). Experimental investigations are made possible by the application FIB-sectioning, which allows detailed cross-sectional analysis of decomposed ceramic samples without modifying sample morphology, with elemental mapping techniques to obtain detailed compositional data of the exposed ceramic sample.

5. Conclusion

- This class of material yields distinct granular and intergranular regions on sintering, each of which undergoes decomposition under moist reducing environments. The grains are barium cerate–zirconate and intergranular region is composed of BaO, CeO_2 and CoO.
- The mottled appearance of the grains at $600\,^\circ\text{C}$ and a uniform appearance at $927\,^\circ\text{C}$ may be explained in terms of the barium cerate hydrolysis mechanism proposed by Tanner and Virkar[19].
- The ex-solution of Co, leading to the formation of BaO, CeO_2 and CoO in the grain boundaries, in conjunction with the hydrolysis of barium cerate–zirconate provides an explanation of the complete disintegration of the intergranular region at $600\,^\circ\text{C}$ and the partial disintegration at $927\,^\circ\text{C}$.
- The reduction of Co, in tandem with the agglomeration under reducing environments, provides an explanation for the formation of highly concentrated, localized, Co-rich regions that are distinct from the original grains.
- The current analysis holds good for Co-doped barium cerate–zirconate with 13 mol% Co doping and an A:B ratio that is >1. The morphology of the material and the pathways of degradation may change with changes in the level of Co doping and the A:B ratio. Thermodynamic analysis of these defects may generate new insight about materials chemistry with enhanced stability.
- FIB-sectioning is a powerful tool that allows the analysis of representative sections of sintered ceramics such that the original morphology of the material is retained under the microscope. This, in conjunction with the advanced microscopic technique of elemental mapping, makes the analysis presented in this paper unique among other similar studies.[19–23] These tools can be used to definitively and efficiently resolve ambiguities regarding the stability of existing materials like barium cerate and to explore stability issues of emerging materials.

Acknowledgements

References

1. Batista MS, Santos RKS, Assaf EM, Assaf JM, Ticianelli EA. High efficiency steam reforming of ethanol by cobalt-based catalysts. *J Power Sources* 2004;**134**:27–32.
2. Tang S, Lin J, Tan KL. Partial-oxidation of methane to synthesis gas over α-Al_2O_3-supported bimetallic Pt–Co catalysts. *Catal Lett* 1999;**59**:129–35.
3. Qi Z, He C, Kaufman A. Effect of CO in the anode fuel on the performance of PEM fuel cell cathode. *J Power Sources* 2002;**111**:239–47.
4. de Briujn FA, Papageorgopoulos DC, Sitters EF, Janssen GJM. The influence of carbon dioxide on PEM fuel cell anodes. *J Power Sources* 2002;**110**:117–24.
5. Harold MP, Nair B, Kolios G. Hydrogen generation in a Pd-membrane fuel processor: assessment of methanol based fuel processor. *Chem Eng Sci* 2003;**58**:2551–71.
6. Huijsmans JPP, van Berkel FPF, Christie GM. Intermediate temperature SOFC—a promise for the 21st century. *J Power Sources* 1998;**71**:107–10.
7. Xia C, Rauch W, Chen F, Liu M. $Sm_{0.5}Sr_{0.5}CoO_3$ cathodes for low-temperature SOFCs. *Solid State Ionics* 2002;**149**:11–9.
8. Iwahara H, Uchida H, Ono K, Ogaki K. Proton conduction in sintered oxides based on $BaCeO_3$. *J Electrochem Soc* 1988;**135**:529–33.
9. Snijkers FMM, Buekenhoudt A, Cooymans J, Luyten JJ. Proton conductivity and phase composition in $BaZr_{0.90}Y_{0.10}O_{3-\delta}$. *Scripta Mater* 2004;**50**:655–9.
10. Yajima T, Suzuki H, Yogo T, Iwahara H. Protonic conduction in $SrZrO_3$-based oxides. *Solid State Ionics* 1991;**51**:101–7.
11. Yajima T, Kazeoka H, Yogo T, Iwahara H. Proton conduction in sintered oxides based on $CaZrO_3$. *Solid State Ionics* 1991;**47**:271–5.
12. Azimova MA, McIntosh S. Transport properties and stability of cobalt doped proton conducting oxides. *Solid State Ionics* 2009;**180**:160–7.
13. Suresh A, Basu J, Carter C Barry, Sammes N, Wilhite BA. Synthesis of cobalt-doped barium cerate–zirconate and its evaluation for hydrogen production and electrochemical characterization. *J Mater Sci* 2010;**45**:3215–27.
14. Lee DW, Won JH, Shim KB. Low temperature synthesis of $BaCeO_3$ nano powders by citrate process. *Mater Lett* 2003;**57**:3346–51.
15. Bhowmick S, Basu J, Xue Y, Barry CC. Hydrothermal synthesis of nanocrystalline barium cerate using hexamethylenetetramine. *J Am Ceram Soc* 2010;**93**:4041–6.
16. Basu J, Divakar R, Winterstein JP, Carter C Barry. Low-temperature and ambient-pressure synthesis and shape evolution of nanocrystalline pure, La-doped and Gd-doped CeO_2. *Appl Surf Sci* 2010;**256**:3772–7.
17. Ranran P, Yan W, Lizhai Y, Zongqiang M. Electrochemical properties of intermediate-temperature SOFCs based on proton conducting Sm-doped $BaCeO_3$ electrolyte thin film. *Solid State Ionics* 2006;**177**:389–93.
18. Katahira K, Kohchi Y, Shimura T, Iwahara H. Proton conduction in Zr-substituted $BaCeO_3$. *Solid State Ionics* 2000;**138**:91–8.
19. Tanner CW, Virkar AV. Instability of $BaCeO_3$ in H_2O-containing atmospheres. *J Electrochem Soc* 1996;**143**:1386–9.
20. Matsumoto H, Kawasaki Y, Ito N, Enoki M, Ishihara T. Relation between electrical conductivity and chemical stability of $BaCeO_3$-based proton conductors with different trivalent dopants. *Electrochem Solid State Lett* 2007;**10**:B77–80.
21. Wu Z, Liu M. Stability of $BaCe_{0.8}Gd_{0.2}O_3$ in a H_2O containing atmosphere at intermediate temperature. *J Electrochem Soc* 1997;**144**:2170–5.

22. Bonano N, Ellis B, Mahmood MN. Construction and operation of fuel cells based on the solid electrolyte $BaCeO_3$:Gd. *Solid State Ionics* 1991;**44**:305–11.

23. Taniguchi N, Yasumoto E, Gamo T. Operating properties of solid oxide fuel cells using $BaCe_{0.8}Gd_{0.2}O_{3-\delta}$ electrolyte. *J Electrochem Soc* 1996;**143**:1886–90.

24. Babilo P, Haile SM. Enhanced sintering of yittrium-doped barium zirconate by addition of ZnO. *J Am Ceram Soc* 2005;**88**:2362–8.

25. Schober T, Bohn HG. Water vapor solubility and electrochemical characterization of the high temperature proton conductor $BaZr_{0.9}Y_{0.1}O_{2.95}$. *Solid State Ionics* 2000;**127**:351–60.

26. Flint SD, Hartmanova M, Jones JS, Slade RCT. Microstructure of Ca-doped barium cerate electrolytes $BaCe_{1-x}Ca_xO_{3-d}$ ($x = 0$, 0.02, 0.05, 0.10 and 0.15). *Solid State Ionics* 1996;**86–88**:679–83.